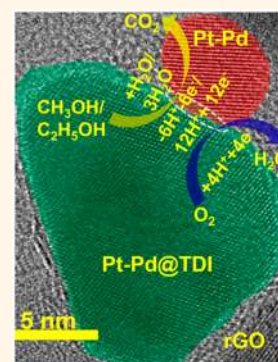# High-Affinity-Assisted Nanoscale Alloys as Remarkable Bifunctional Catalyst for Alcohol Oxidation and Oxygen Reduction Reactions

Jitendra N. Tiwari, Wang Geun Lee, Siraj Sultan, Muhammad Yousuf, Ahmad M. Harzandi, Varun Vij, and Kwang S. Kim*

Department of Chemistry, Ulsan National Institute of Science and Technology (UNIST), 50 UNIST-gil, Ulsan 44919, Korea

S *Supporting Information*

ABSTRACT: A key challenge in developing fuel cells is the fabrication of low-cost electrocatalysts with high activity and long durability for the two half-reactions, *i.e.*, the methanol/ethanol oxidation reaction (MOR/EOR) and the oxygen reduction reaction (ORR). Herein, we report a conductivity-enhanced bifunctional electrocatalyst of nanoscale-coated Pt−Pd alloys on both tin-doped indium (TDI) and reduced graphene oxide (rGO), denoted as Pt−Pd@TDI/rGO. The mass activities of Pt in the Pt−Pd@TDI/rGO hybrid toward MOR, EOR, and ORR are 2590, 1500, and 2690 mA/mg, respectively. The ORR Pt specific activity and mass activity of the electrocatalyst are 17 and 28 times larger, respectively, than commercial Pt/C catalysts. All these remarkable catalytic performances are attributed to the role of TDI in enhancing the catalytic activity by protecting Pt from oxidation as well as rapid mass/charge transfer due to the synergistic effect between surface Pt−Pd alloys and TDI/rGO.

Developing highly efficient, low-cost, and durable hybrid catalysts is vital for the design of practical and futuristic fuel cells that transform chemical energy into electrical energy with high efficiency.[1−3] Among various types of proton exchange membrane fuel cells (PEMFCs), the liquid-feed fuel cells (LFFCs) such as direct-methanol fuel cells and direct-ethanol fuel cells have attracted considerable attention due to their low cost and safe, easy storage/transfer of liquid methanol/ethanol.[4] More importantly, unlike hydrogen PEMFCs, the LFFCs based on methanol/ethanol do not require humidification and thermal management. Platinum (Pt) is still the most effective catalyst for methanol/ethanol oxidation reaction (MOR/EOR; anode) and oxygen reduction reaction (ORR; cathode) in an LFFC. Therefore, it is still difficult to replace Pt with an alternative candidate.[5,6] However, the MOR/EOR/ORR performed on Pt at the anode/cathode suffers from CO poisoning, poor oxidation, sluggish kinetics, instability of the Pt catalysts, and particle ripening and dissolution.[7−10] Therefore, major research efforts are under way to reduce the use of Pt catalysts in catalytic processes without losing their activity and stability.[11−13]

The unfavorable activity and stability of Pt catalysts are ascribed to the corrosion of electrodes.[14] Due to the corrosion at the anodes and cathodes, the electrochemically active surface area (ESA) of the Pt nanoparticles decreases, which reduces the MOR/EOR/ORR activities and therefore deteriorates the fuel

cell performance. The harsh conditions, particularly at the cathode side, are due to an acidic environment with high oxygen concentration and high water content.[14] To date, no promising electrode materials are available for LFFCs. Nevertheless, one effective approach is to increase the catalytic efficiencies (activity and stability) by alloying Pt with other metal oxide nanoparticles.[15−17] Multimetallic nanoparticles constitute another class of materials that offer the opportunity to tune their properties by varying their composition, atomic ordering, and size.[18−20]

In this study, we report a highly conductive bifunctional electrocatalyst, Pt−Pd@TDI/rGO (TDI, tin-doped indium; rGO, reduced graphene oxide), with outstanding electrochemical properties and long-term stability. Its notable mass and specific activities for MOR/EOR/ORR in an acidic electrolyte, as well as its durability, are attributed to the strong chemical interaction between Pt−Pd alloys and TDI nanoparticles/rGO, which results in a fast charge-transfer rate. Moreover, the junction between Pt−Pd@TDI/rGO particles and Pt−Pd alloys helps to avoid aggregation and dissolution of the catalyst by suppressing the oxidation of Pt and Pd to ensure
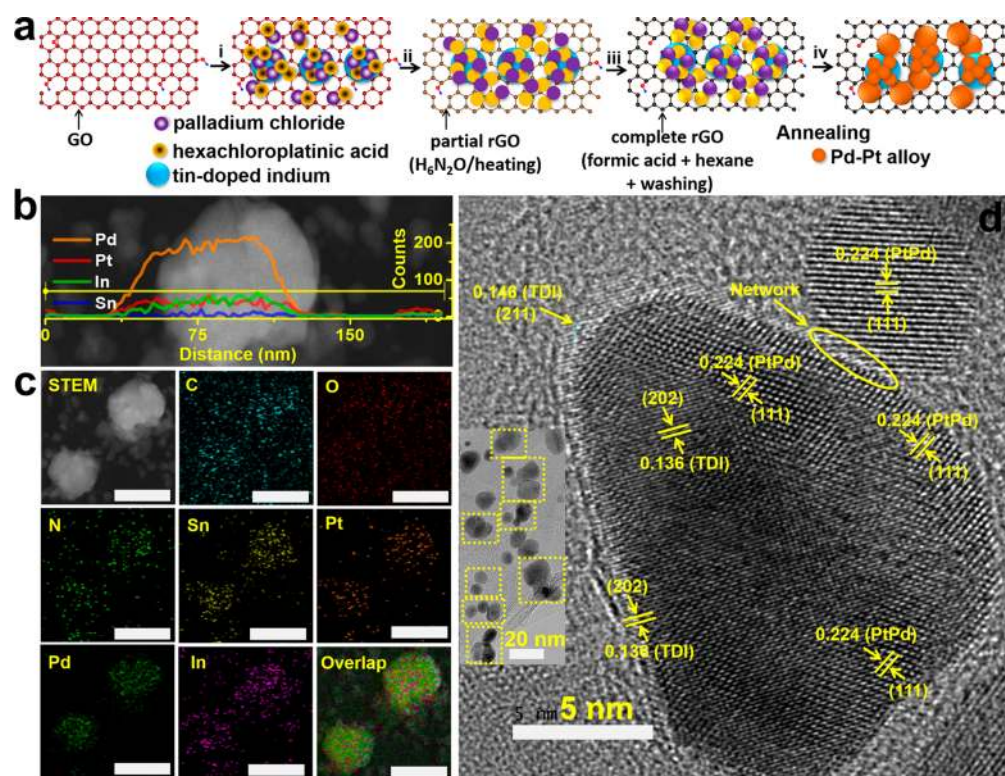
Figure 1. Synthesis and physical characterization of Pt−Pd@TDI/rGO electrocatalysts. (a) Schematic of synthetic procedure: (i) mixing graphene oxide (GO), palladium chloride, hexachloroplatinic acid, and tin-doped indium (TDI) using sonication, (ii) adding hydrazine hydrate and heating at 100 °C, (iii) adding formic acid and hexane for complete reduction and washing, and (iv) two-step annealing at 500 °C. (b) STEM image and the cross-sectional compositional line scanning profiles along the direction marked by a yellow line in (b). (c) STEM-EDS elemental mapping of C, O, N, Sn, Pt, Pd, and In, along with an overlapped image. (d) Bright-field TEM (inset) and HRTEM images. Scale bar in (c): 50 nm.

clean surfaces over a wide potential range. Our studies show that the TDI nanoparticles/rGO hybrid not only minimizes Pt and Pd usage but also significantly enhances the CO tolerance of the catalyst and, thus, greatly enhances its durability, making it a promising candidate for future fuel cell applications.

RESULTS AND DISCUSSION

The synthetic strategy for the Pt−Pd@TDI/rGO hybrid is illustrated in Figure 1a (see Experimental Section). Representative high-resolution high-angle annular dark-field scanning transmission electron microscope (HAADF-STEM) images of the as-synthesized Pt−Pd@TDI/rGO hybrid are shown in Figure 1b. The line-scan energy-dispersive X-ray spectroscopy (EDX) spectra of elemental Pt, Pd, In, and Sn were recorded through the center of a single particle (Figure 1b inset). The compositional line-scan profiles of Pt, Pd, In, and Sn on individual particles show a consecutive variation without any segregation of each component. This reveals that the Pt−Pd@TDI/rGO hybrid indeed contains PtPd@TDI alloys. The signals of the Pt, Pd, In, and Sn fluctuate along the scanning direction, which indicates that the Pt and Pd atoms are randomly distributed on the surface of the TDI particles. Scanning transmission electron microscopy (STEM)-EDX mapping (Figure 1c) shows that pure Pd/Pt atoms or nanoparticles and Pt−Pd alloys are deposited on the surface of TDI/rGO. The transmission electron microscopy (TEM) image shows the Pt−Pd alloy particles joined with TDI in the Pt−Pd@TDI hybrid (Figure 1d inset). The formation of junctions between Pt−Pd alloys and TDI nanoparticles is also

confirmed by the high-resolution TEM (HRTEM) image (Figure 1d). These junctions provide excellent electrical contacts between the sites of oxidation and reduction, resulting in fast electron transfer in the reactions, which leads to remarkable catalytic features. The TDI and Pt−Pd alloys display clear fringes in the HRTEM image (Figure 1d) with lattice spacings of 0.136 nm (corresponding to the {202} plane) and 0.224 nm (corresponding to the {111} plane), confirming the highly crystalline character of the multimetallic alloy nanoparticles.

The X-ray diffraction (XRD) patterns of Pt−Pd@TDI/rGO (annealed), unannealed Pt−Pd@TDI/rGO (Pt−Pd@TDI/rGO-0), and Pt−Pd/rGO can be indexed as a face-centered cubic (fcc) structure (Figure S1). The XRD patterns of Pt−Pd@TDI/rGO and Pt−Pd/rGO catalysts display the Pt(111) peak, which is slightly shifted to higher 2θ values, confirming the alloy formation in Pt−Pd catalysts due to the incorporation of Pd atoms into the Pt fcc lattice. However, no obvious peak shift was observed in the Pt−Pd@TDI/rGO-0 catalyst, indicating that the Pt−Pd alloy was not formed before annealing. All the catalysts show a peak at ∼25°, which is assigned to the rGO support, and the patterns for all TDI-incorporated catalysts exhibit the diffraction peak of TDI. The inductively coupled plasma atomic emission spectroscopy (ICP-AES) analysis indicates that the contents of Pd and Pt are 5.7 and 3.6 wt %, respectively, which is fully consistent with the X-ray photoelectron spectroscopy (XPS) compositional analysis (Table S1). The full-survey XPS spectra (Figure S16)

clearly indicate the existence of Pt, Pd, In, Sn, and C elements in the Pt−Pd@TDI/rGO hybrid.

From the XPS core-level spectra, the In 3d peaks (Figure 2a) split into two strong peaks at 444.7 eV (In $3d_{5/2}$) and 452.2 eV
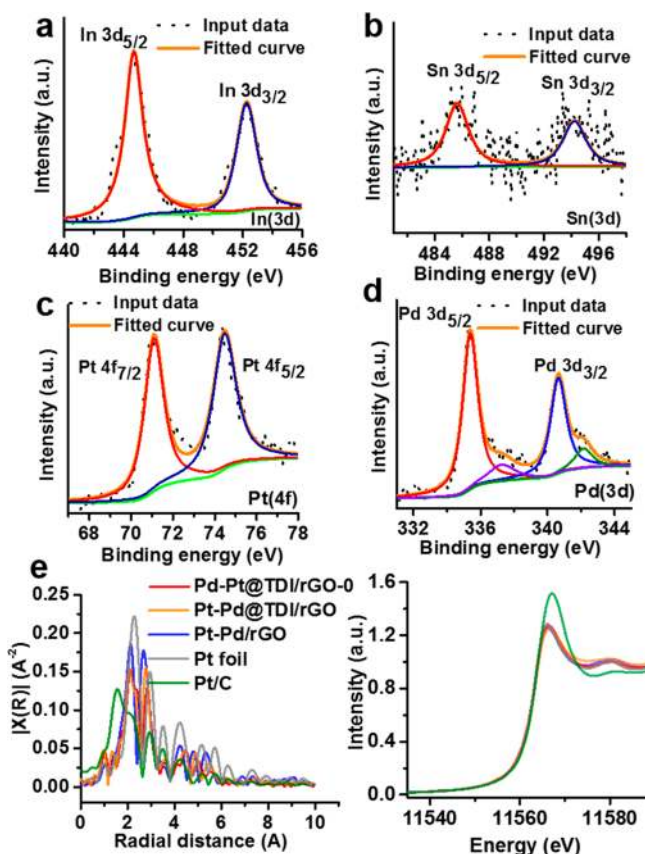

Figure 2. Chemical analysis. (a−d) Experimental and fitted high-resolution XPS spectra of In 3d (a), Sn 3d (b), Pt 4f (c), and Pd 3d (d) core levels for Pt−Pd@TDI/rGO electrocatalysts. (e) Fourier transform k_1-weighted EXAFS spectra and the corresponding normalized XANES spectra at the Pt K-edge.

(In $3d_{3/2}$), which correspond to those reported for In_2O_3 particles.[21] The Sn 3d spectrum shows two strong peaks of Sn $3d_{5/2}$ (485.6 eV) and Sn $3d_{3/2}$ (494.2 eV) with a spin−orbit splitting of 8.6 eV (Figure 2b). The observed binding energy values of the Sn 3d peaks indicate that Sn is in the +4 valence state.[22] We have measured the Pt 4f binding energy (Pt $4f_{7/2} \approx$ 71.2 eV and Pt $4f_{5/2} \approx$ 74.5 eV) for the Pt−Pd@TDI/rGO hybrid (Figure 2c), which suggests that Pt is in the pure metallic state (Pt in the zero-valence state).[23,24] The Pd 3d sub-band (Figure 2d) shows two strong peaks of Pd $3d_{5/2}$ (~335.4 eV) and Pd $3d_{3/2}$ (~340.7 eV), which correspond to bulk Pd metal.

The Fourier transform extended X-ray absorption fine structure (FT-EXAFS) data of all the catalysts exhibit two main peaks of ~2 and ~3 Å at the Pt L_3 edge, which is attributed to the phase-uncorrected first-shell interactions of Pt−M (M = Pt or Pd; Figure 2e). It should be noted that the peak amplitude of all the catalysts is lower than that of Pt foil, which is due to the smaller size of nanoparticles, resulting in a decrease in the average coordination number relative to Pt foil. More interestingly, we observe significant changes in Pt−Pt bond distance introduced by Pd and TDI. The Pt−Pt bond distance of the Pt−Pd@TDI/rGO hybrid (~2.79 Å) is 0.16 Å

less than that of Pt foil (~2.95 Å), which is ascribed to alloying, electronic, and synergistic effects of the hybrid catalysts.[25] X-ray absorption near-edge structure (XANES) spectra provide the local electronic and geometric structures of X-ray absorbing atoms of the hybrid catalysts. The XANES curve shapes at the Pt L_3 edge for all the rGO-based samples are similar to those of the corresponding Pt foil (Figure 2e), indicating that the local order of Pt in rGO-based catalysts is still Pt metal-like, which agrees with the aforementioned results by XPS.

The surface properties and molecular structures of GO, Pt/rGO, Pt−Pd/rGO-0 (unannealed), Pt−Pd/rGO, Pt−Pd@TDI/rGO-0 (unannealed), and Pt−Pd@TDI/rGO hybrids were characterized using Fourier transform infrared (FTIR) spectra (Figure S2). The structural changes occurring during the chemical processing of GO to TDI/rGO to Pt−Pd@TDI/rGO were confirmed by their Raman spectra (Figure S3). The Pt−Pd@TDI/rGO hybrid exhibits a remarkable catalytic activity toward MOR/EOR/ORR in an acidic electrolyte (Figures 3, 4). Hereafter, we discuss only the catalytic properties of Pt−Pd@TDI/rGO, Pt−Pd/rGO, and state-of-the-art carbon-supported commercial Pt/C due to their exemplary activity.

To directly compare the methanol and ethanol electro-oxidation activity of Pt−Pd@TDI/rGO with Pt/C and Pt−Pd/rGO, we obtained cyclic voltammograms (CVs) in 0.1 M $HClO_4$ solution containing methanol/ethanol (Figure 3a−d). A high peak-current mass activity was obtained for methanol/ethanol electro-oxidation (~2590/1500 mA·mgPt^{-1}) with Pt−Pd@TDI/rGO (Figure 3a,c). However, for Pt/C (~900/800 mA·mgPt^{-1}) and Pt−Pd/rGO (~600/90 mA·mgPt^{-1}), small methanol/ethanol electro-oxidation peaks with low-current mass activity were observed (Figure 3a,c), indicating that the methanol/ethanol electro-oxidation was less active. It is clear to see that Pt−Pd@TDI/rGO gives the highest current density, which is ~2.9 and ~4.3 times (in methanol) and ~1.9 and ~16 times (in ethanol) higher than those of Pt/C and Pt−Pd/rGO, respectively. The current mass activity of Pt−Pd@TDI/rGO is also much higher than a recently reported value (Table S2). Additionally, in the case of EOR, the first peak at 0.99 V (versus the reversible hydrogen electrode; RHE) is due to the oxidation of ethanol, whereas the second peak at 1.34 V (versus RHE) can be ascribed to side products such as acetaldehyde and acetic acid.[26] The ratio of the forward to backward peak currents (I_f/I_b) during methanol oxidation is used to indicate the CO tolerance of the catalyst, with a higher I_f/I_b ratio indicating better CO tolerance.[27] At different CV cycles, the I_f/I_b ratio for Pt−Pd@TDI/rGO is much higher than those for Pt−Pd/rGO and Pt/C (Figure 3b). The onset potential is related to the breaking of the C−H bonds and the subsequent removal of CO through oxidation by adsorbed OH species.[28] The onset potential for Pt−Pd@TDI/rGO (0.58 V) is lower than those for Pt−Pd/rGO (0.61 V) and Pt/C (0.66 V) (Figure 3a). The excellent CO tolerance of Pt−Pd@TDI/rGO was further confirmed by CO stripping tests in 0.1 M $HClO_4$. Pt−Pd@TDI/rGO has the highest peak potential of 0.878 V (versus RHE), which is more negative than those of Pt−Pd/rGO (1.11 V versus RHE, 232 mV shift) and Pt/C (0.907 V versus RHE, 29 mV shift) (Figure S4). The notable CO tolerance is attributed to the oxygen at the surface of the metallic oxide alloyed with Pt, which can oxidize the poisonous CO species to CO_2, thus cleaning the catalyst surface.

By using hydrogen adsorption−desorption methods in conjunction with CV, the ESA of Pt−Pd@TDI/rGO (124.6
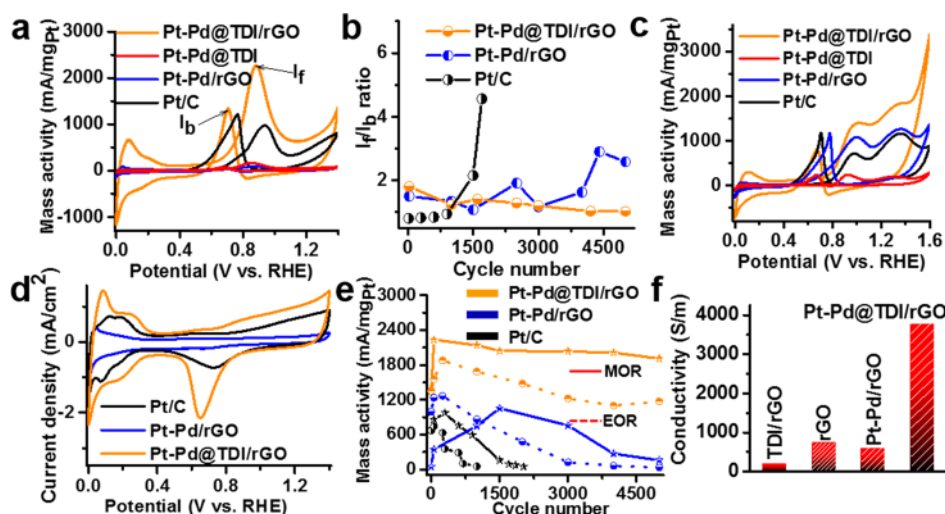
Figure 3. Alcohol oxidation performance. (a) Cyclic voltammograms (CVs) of Pt–Pd@TDI/rGO in a 0.1 M HClO$_4$ + 0.5 M CH$_3$OH solution at a scan rate of 50 mV/s. (b) Ratio of forward to backward peak currents (I_f/I_b) for different CV cycles. (c) CVs of Pt–Pd@TDI/rGO in a 0.1 M HClO$_4$ + 0.5 M C$_2$H$_5$OH solution at a scan rate of 50 mV/s. (d) Room-temperature CV curves for electrocatalysts in a N$_2$-saturated 0.1 M HClO$_4$ solution at a scan rate of 50 mV/s. (e) Mass activity (methanol/ethanol oxidation reactions; MOR/EOR) for different CV cycles. (f) Conductivity for different electrocatalysts.
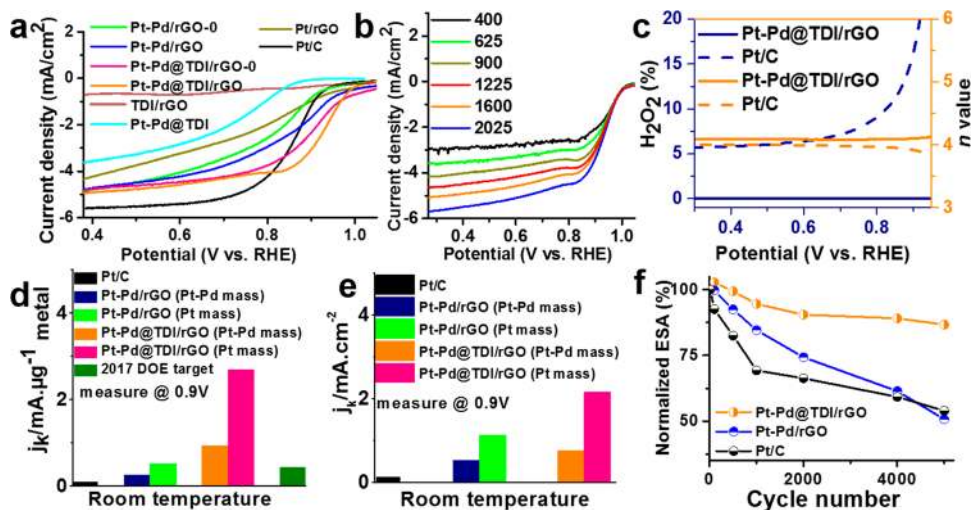

Figure 4. Oxygen reduction performance. (a) Room-temperature rotating disk electrode (RDE) measurement curves for electrocatalysts in an O$_2$-saturated 0.1 M HClO$_4$ solution at a scan rate of 10 mV/s after background subtraction measured with a N$_2$-saturated 0.1 M HClO$_4$ solution. (b) Room-temperature RDE measurement curves for Pt–Pd@TDI/rGO in an O$_2$-saturated 0.1 M HClO$_4$ solution at a scan rate of 10 mV/s and different rotation speeds corrected by subtracting background from a N$_2$-saturated solution. (c) H$_2$O$_2$ yield for the oxygen reduction reaction and number of electrons transferred (n) measured with a rotating ring-disk electrode. (d, e) Mass activity (d) and specific activity (e) at 0.9 V *versus* the reversible hydrogen electrode for different electrocatalysts. Mass and specific activities are given as kinetic current densities (j_k) normalized to the loading amount and ESA of Pt and Pt–Pd metals, respectively. In (a), the current density is normalized with reference to the geometric area of the RDE. (f) ESA losses for catalysts in an O$_2$-saturated 0.1 M HClO$_4$ solution at a scan rate of 50 mV/s.

m^2/g) was found to be much larger than those of the commercial Pt/C catalyst (74.2 m^2/g) and Pt–Pd/rGO (46.3 m^2/g) (Figure 3d). This observation is most likely a result of the particular structure of the bimetallic nanoparticles and their homogeneous dispersion on the rGO sheets and TDI, which exhibit a large surface area (see TEM and HRTEM images of the samples).

The higher stability of the Pt–Pd@TDI/rGO hybrid over commercial Pt/C and Pt–Pd/rGO was revealed in 5000 CV cycle tests (Figure 3e). The mass activity had no obvious change for Pt–Pd@TDI/rGO after 5000 CV cycles, which confirmed its excellent durability. In contrast, a continuous

change in the mass activity for commercial Pt/C was clearly observed. The good stability of the hybrid could be ascribed to the strong interactions between Pt–Pd and TDI, which prevent Pt–Pd alloy particles from leaching off and aggregating during methanol/ethanol oxidation. Moreover, the Pt–Pd@TDI/rGO hybrid shows enhanced electrical conductivity (Figure 3f) due to shrinkage of the Pt–Pt atomic distance, resulting in facile electron transfer in the reaction, which leads to better catalytic properties.

Polarization curves for the ORR of the "annealed" Pt–Pd@TDI/rGO and Pt–Pd/rGO electrocatalysts show higher ORR efficiencies compared with commercial Pt/C and other catalysts

(Figure 4a). Pt−Pd@TDI/rGO has a higher ORR onset potential (~1.03 V) than Pt−Pd/rGO, and this value is ~80 mV higher than that of Pt/C. In general, the electrocatalytic activities of an ORR catalyst are evaluated by the half-wave potential ($E_{1/2}$) of its ORR polarization curve. $E_{1/2}$ increases in the order Pt/C < Pt−Pd/rGO < Pt−Pd@TDI/rGO (Figure 4a,b). Pt−Pd@TDI/rGO shows a remarkable positive $E_{1/2}$ shift of ~65 mV relative to Pt/C, implying a significant increase in the ORR activity. These linear sweep voltammetry curves reveal that the ORR kinetics are dramatically accelerated on dealloyed Pt−Pd nanoparticles, especially the dealloyed Pt−Pd on the TDI surface, relative to Pt/C. The kinetic current (I_k) was calculated using the Koutecky−Levich (K-L) equation (see Methods in the Supporting Information). The number of electrons transferred (n) is ~4.1 between 0.825 and 0.900 V from the slopes of the K-L plots (Figure S5), which matches well with the rotating ring-disk electrode measurement result ($n \approx 4.1$; Figure 4c). These results indicate the complete reduction of O_2 to H_2O on the surface of Pt−Pd@TDI/rGO. A similar number of electrons was calculated for the Pt/C catalyst at potentials between 0.775 and 0.85 V (Figure 4c, Figure S6).

Pt−Pd@TDI/rGO exhibits a remarkable mass electro-catalytic activity (~2.69 mA/μg$_{Pt}$ and ~0.94 mA/μg$_{Pt-Pd}$ at 0.9 V) for ORR (Figure 4d, Table S3), which is even higher than the target value (0.44 mA/μg$_{Pt}$ at 0.9 V) set by the U.S. Department of Energy (DOE) for 2017.[29,30] The specific activity (j_k) of Pt−Pd@TDI/rGO is ~2.15 mA/cm$^2_{Pt}$ (~0.76 mA/cm$^2_{Pt-Pd}$ at 0.9 V), much higher than those of Pt/C, Pt−Pd/rGO, and other reported catalysts (Figure 4e). The ORR activity of the hybrid shows more than 28 times increase in Pt mass activity relative to commercial Pt/C catalysts. The significant increase in specific activity suggests that the Pt−Pd dealloyed surface on TDI particles exhibits surface electronic properties that are favorable for ORR.

Accelerated durability tests of the electrocatalysts were performed by cycling the potential between 0.6 and 1.4 V *versus* RHE for 5000 cycles in an O_2-saturated 0.1 M HClO$_4$ solution at a scan rate of 50 mV s^{-1}. A large potential window (1.4 V) was used as the upper threshold potential to ensure surface oxidation/reduction cycles on Pt/Pd, which involves the formation of PtOH and PtO derived from oxidation of water. This causes the dissolution of Pt/Pd.[31] High-potential treatment also mimics fuel cell startup/shutdown conditions in which commercial Pt/C electrocatalysts suffer from very poor stability.[32] In the CVs of the Pt−Pd@TDI/rGO hybrid (Figure S7a), well-defined hydrogen adsorption/desorption peaks appear with high ESA after the 10th ~5000 cycles. With continued cycling, the hydrogen adsorption/desorption peaks continuously decrease from the first to the 5000th cycle (Figure 4f). This suggests that the catalytic behavior of Pt−Pd@TDI/rGO is initially dominated by Pt−Pd@TDI, and the TDI particles gradually leach away, exposing more Pt on the surface. This result agrees with our bright-field TEM and EDX elemental mapping images, which indicate a small amount of hollowing in the TDI particles due to leaching of Sn from In after 5000 cycles (Figures S8, S9). However, this is not the case for Pt−Pd/rGO (ESA decreases by ~49% after 5000 cycles) and Pt/C (ESA decreases by ~46% after 5000 cycles). In both samples, the area with catalytic activity decreases with cycling due to detachment/agglomeration of Pt particles on the surface of the carbon or rGO (Figures S10 and S11).

In contrast, for Pt−Pd@TDI/rGO, the ESA decreases by ~13% of the initial value after ~5000 cycles (Figure 4f). After 5000 potential cycles, Pt−Pd/rGO and Pt/C show degradation of more than ~60 and ~55 mV in $E_{1/2}$, respectively (Figures S10b, S11b), whereas the degradation of Pt−Pd@TDI/rGO is much lower with a negative shift in $E_{1/2}$ of less than ~10 mV (Figure S7b). Furthermore, most of the particles were still homogeneously dispersed on the TDI and rGO support (Figures S8, S9). The structural stability of Pt−Pd@TDI/rGO after 5000 electrochemical cycles is verified by bright-field TEM and elemental mapping images (Figures S8, S9). The Pt−Pd alloys neither coalesced/aggregated nor dissolved due to the continuous removal of oxides from the Pt or Pd surface through TDI,[33] we consider three electrochemical reactions for Pt dissolution: (1) Pt = Pt^{2+} + 2e$^-$, (2) Pt oxide film formation, Pt + H$_2$O = PtO + 2H$^+$ + 2e$^-$, and (3) chemical dissolution of Pt oxide, PtO + 2H$^+$ = Pt^{2+} + H$_2$O. From the bright-field TEM images, line scanning profiles, and elemental mapping of Pt−Pd@TDI/rGO before and after 5000 potential cycles (Figure 1b−d, Figures S8, S9), the Pt−Pd alloy clearly exists without aggregation/dissolution of Pt on the rGO surface (Figures S8, S9), thus displaying good long-term operation stability.

The reason that we used rGO, Pt/Pd, and TDI and the way their amounts were optimized are as follows. (i) Since rGO is a conductive substrate material, we used it as our starting precursor, and the ratio of other three components (Pt, Pd, and TDI) was discretely taken in reference to rGO. (ii) Pt is a well-established metal to exhibit phenomenal electrocatalytic performance in oxygen reduction. The role of Pd is not only to increase the mass activity (with respect to Pt) of catalyst by decreasing the relative amount of Pt but also to obstruct the agglomeration of Pt nanoparticles during the electrochemical course. Therefore, we optimized the ratio of Pt:Pd by varying different weight proportions of both metals with respect to rGO. We achieved the best catalytic activity by using a Pt:Pd weight percent ratio of 5.5:6.04 with respect to 87% of carbon. Any increase or decrease in the aforementioned composition resulted in a decrease in the performance of catalyst. (iii) The indium oxide favorably influences the oxidation and reduction behavior of the supported Pt by suppressing the formation of Pt-oxide species at high potentials, which can otherwise easily dissolve in the electrolyte. However, the overall conductance of the material can be adversely affected due to poor conductivity of indium oxide, which was avoided by appropriate amount of Sn-doping. A controlled Sn-doping into indium oxide can significantly enhance the electrical conductivity of hybrid material Pt−Pd@TDI/rGO by introducing the synergistic effect between generated Sn−O defects and the binary alloy of Pt/Pd. Initially, the increase in ratio of TDI with respect to rGO in the hybrid material Pt−Pd@TDI/rGO resulted in enhancement in its catalytic property toward MOR, EOR, and ORR. A further increase in ratio of TDI increases neither the degree of surface adsorption nor the catalytic activity of the hybrid material Pt−Pd@TDI/rGO due to saturation of the available binding sites on the surface of rGO.

CONCLUSIONS

In summary, we have developed an easy procedure to synthesize bifunctional Pt−Pd@TDI/rGO hybrids for alcohol electro-oxidation and ORRs. The mass activity of these hybrids can increase to 2.6/1.5 A mg$^{-1}_{Pt}$ for methanol/ethanol oxidation in acidic solutions, which is 2.9/1.9 and 4.3/16 times greater than those of commercial Pt/C and Pt−Pd/rGO,

respectively. The Pt−Pd@TDI/rGO hybrid shows much better long-term stability than the commercial Pt/C and Pt−Pd/rGO. More significantly, with respect to the 2017 U.S. DOE target values, the as-synthesized Pt−Pd@TDI/rGO hybrid shows exceptionally good ORR catalytic activities in terms of onset potential, half-wave potential, specific activity, mass activity, poisoning tolerance, low cost, and durability. Its remarkable activity and durability could be ascribed to the synergistic effect between the surface Pt−Pd and the TDI alloy, and the collective functions of the four components (Pt, Pd, TDI, and rGO) contribute to the high catalytic activity of the Pt−Pd@TDI/rGO hybrid. Thus, only a low amount of Pt was required to produce high currents, which reduced the use of noble metals. These results indicate that the Pt−Pd@TDI/rGO hybrid is a promising electrocatalyst for fuel cells.

EXPERIMENTAL SECTION

Synthesis of Tin-Doped Indium. A white slurry of indium acetyl acetonate (1.25 g, 3.07 mmol) and tin bis(acetylacetonate) dichloride (0.061 g, 0.161 mmol) in 50 mL of olylamine is prepared. The slurry has a Sn content of 6 wt %. The slurry is then heated at 150 °C for 4 h; afterward the temperature was increased up to 250 °C and stirring was continued for an additional 12 h to produce a dark yellow suspension. The TDI nanoparticles were precipitated by adding absolute ethanol (100 mL) to the suspension. This mixture was centrifuged at 10 000 rpm for 10 min, and the supernatant was discarded. The remaining TDI nanoparticles were then washed with ethanol four times and heated at 100 °C under vacuum for 24 h. Finally, the dried powder was annealed at 500 °C for 5 h under argon. The structure of the TDI nanoparticles was examined using scanning electron microscope (SEM) (Figure S13). TEM and HRTEM were utilized to observe the crystallinity of the TDI powder (Figure S14). From these images, the uncrystallized and crystallized structure before and after annealing at 500 °C were clearly observed (Figure S14a,b). The controlled temperature treatment assists in growth and rearrangement of the lattice structure of the nanoparticles with high surface energy, resulting in transformation into a more stable crystalline structure.[30] The XRD spectra of TDI nanoparticles display the four characteristic peaks of (101), (110), (200), and (211), indicating the doping of Sn into In_2O_3 (JCPDS 01-073−-9038) (Figure S15a). Moreover, the full-survey XPS spectra also confirm the presence of In and Sn elements in TDI nanoparticles (Figure S15b).

Synthesis of Pt−Pd@TDI/rGO and Pt−Pd/rGO Hybrids. GO (30 mg) was dispersed in distilled water by sonication for 6 h. To this dispersion were added TDI (20 wt % of GO), hexachloroplatinic acid (15 wt % of GO), and palladium chloride (15 wt % of GO), and the resulting solution was sonicated for 6 h. To this mixture was added hydrazine hydrate (5 mL), and the mixture was refluxed for 24 h. Finally, formic acid (7 mL) and hexane (5 mL) were added to complete the reduction of the metal complex. The whole mixture was then filtered and washed repeatedly (five times) with distilled water. The solid was then heated at 100 °C under vacuum to obtain the desired product. The dried samples were annealed at 500 °C under argon. The annealed samples with and without TDI are assigned as Pt−Pd@TDI/rGO and Pt−Pd/rGO, respectively, while those without annealing are assigned as PD@TDI/rGO-0 and Pt−Pd/rGO-0.

Physical Characterizations. To prepare the GO atomic force microscopy (AFM) sample, a GO solution was drop cast onto a Si surface. AFM images were recorded using an atomic force microscope, Veeco Dimension 3100 Ambient AFM. Micro-Raman measurement was performed using a Senterra Raman Scope system with a 532 nm wavelength incident laser light and 20 mW power. The morphologies of the synthesized samples were characterized using a field-emission SEM (JEOL, FEG-XL 30S) with an acceleration voltage of 5 kV. The Pt and Pd composition of the catalysts was measured by an ICP-AES system. The morphology and chemical composition of the samples were characterized on a JEM-2200FS (Cs-corrected STEM) HRTEM coupled with an EDX spectrometer (Dxford-1NCA) at an acceleration

voltage of 200 kV. The STEM imaging and elemental mappings were acquired on a scanning transmission electron microscope unit with HAADF. Contact angle measurements of the as-synthesized samples were carried out using a surface electro-optics apparatus (SEO, Phoenix 300).

Electrochemical Cyclic Voltammetry Analysis. The electrochemical measurements were performed on an electrochemical workstation (CHI 760E, CH Instruments Inc.) at room temperature, using a three-electrode electrochemical setup, which consisted of a Pt wire as counter electrode, a Ag/AgCl (3 M NaCl) electrode as reference electrode, and a modified glassy carbon electrode (5 mm in diameter) as substrate for the working electrode. The ESAs were determined by integrating the hydrogen adsorption/desorption area in the CV curves. The oxidation charge for a monolayer of adsorbed H on a Pt surface is assumed to be 210 μC cm^{-2}. To examine the MOR and EOR electrocatalytic stability of the as-prepared catalysts, electrochemical experiments were performed by 250 CV cycles in N_2-saturated 0.1 M $HClO_4$ containing 0.5 M methanol or ethanol solution at a scan rate of 50 mV s^{-1}. The potentials were normalized to RHE. The mass activities in the cyclic voltammograms were normalized to the loading amount of Pt metals to evaluate the catalytic properties.

Rotating Ring Disc Electrode and a Rotating Disc Electrode Measurements. A three-electrode system was used with a Ag/AgCl reference electrode (3 M NaCl), a Pt counter electrode, a rotating disc electrode (RDE) and a rotating ring disc electrode (RRDE, PINE AFE7R9GCPT) (Pine Instruments, Inc.) as the working electrodes. The diameters of the RDE and RRDE with a ring made of Pt were 5.61 (glassy carbon disk area = 0.247 cm^2) and 6.25 mm, respectively. In our study, a Pt ring with a collection efficiency of 37% was used. The polarization curves for ORR were obtained for the thin film electrocatalysts on an RDE in an O_2-saturated 0.1 M $HClO_4$ solution at 1600 rpm. For the initial ORR activity testing, all electrodes were pretreated by cycling the potential between 0.00 and 1.4 V at a sweep rate of 100 mV s^{-1} for 10 cycles to remove surface contamination. Linear sweep voltammograms were recorded by scanning the disk potential from 1.1 to 0.25 V (*versus* RHE) at a scan rate of 10 mV s^{-1}. High-purity nitrogen or oxygen was used for deaeration of the solutions, and during the measurement, a gentle gas flow was maintained above the electrolyte solution.

Sample Preparation for Physicochemical Characterization. All samples for Raman were prepared by depositing a thin film of the sample on a glass microscope slide at room temperature. Samples for FTIR were made by mixing a small amount of as-synthesized sample with potassium bromide powder and pressing into pellets in a die.

ASSOCIATED CONTENT

Ⓢ Supporting Information

The Supporting Information is available free of charge on the ACS Publications website at DOI: 10.1021/acsnano.7b01073.

Methods, text, analysis, and table (PDF)

AUTHOR INFORMATION

Corresponding Author

*E-mail: kimks@unist.ac.kr.

ORCID Ⓞ

Kwang S. Kim: 0000-0002-6929-5359

Notes

The authors declare no competing financial interest.

ACKNOWLEDGMENTS

REFERENCES

(1) Debe, M. K. Electrocatalyst Approaches and Challenges for Automotive Fuel Cells. *Nature* **2012**, *486*, 43−51.

(2) Myung, J.-H.; Neagu, D.; Miller, D. N.; Irvine, J. T. S. Switching on Electrocatalytic Activity in Solid Oxide Cells. *Nature* **2016**, *537*, 528−531.

(3) Bashyam, R.; Zelenay, P. A Class of Non-precious Metal Composite Catalysts for Fuel Cells. *Nature* **2006**, *443*, 63−66.

(4) Long, N. V.; Yang, Y.; Thi, C. M.; Minh, N. V.; Cao, Y.; Nogami, M. The Development of Mixture, Alloy, and Core-Shell Nanocatalysts with Nanomaterial Supports for Energy Conversion in Low-Temperature Fuel Cells. *Nano Energy* **2013**, *2*, 636−676.

(5) Bu, L.; Guo, S.; Zhang, X.; Shen, X.; Su, D.; Lu, G.; Zhu, X.; Yao, J.; Guo, J.; Huang, X. Surface Engineering of Hierarchical Platinum-Cobalt Nanowires for Efficient Electrocatalysis. *Nat. Commun.* **2016**, *7*, 11850.

(6) Escudero-Escribano, M.; Malacrida, P.; Hansen, M. H.; Vej-Hansen, U. G.; Velázquez-Palenzuela, A.; Tripkovic, V.; Schiøtz, J.; Rossmeisl, J.; Stephens, I. E. L.; Chorkendorff, I. Tuning the Activity of Pt Alloy Electrocatalysts by Means of the Lanthanide Contraction. *Science* **2016**, *352*, 73−76.

(7) Tong, Y. Y. J.; Kim, H. S.; Babu, P. K.; Waszczuk, P.; Wieckowski, A.; Oldfield, E. An NMR Investigation of Co Tolerance in a Pt/Ru Fuel Cell Catalyst. *J. Am. Chem. Soc.* **2002**, *124*, 468−473.

(8) Li, Q.; Wen, X.; Wu, G.; Chung, H. T.; Gao, R.; Zelenay, P. High-Activity PtRuPd/C Catalyst for Direct Dimethyl Ether Fuel Cells. *Angew. Chem., Int. Ed.* **2015**, *54*, 7524−7528.

(9) Nie, Y.; Li, L.; Wei, Z. Recent Advancements in Pt and Pt-free Catalysts for Oxygen Reduction Reaction. *Chem. Soc. Rev.* **2015**, *44*, 2168−2201.

(10) Fang, B.; Chaudhari, N. K.; Kim, M.-S.; Kim, J. H.; Yu, J.-S. Homogeneous Deposition of Platinum Nanoparticles on Carbon Black for Proton Exchange Membrane Fuel Cell. *J. Am. Chem. Soc.* **2009**, *131*, 15330−15338.

(11) Georgakilas, V.; Tiwari, J. N.; Kemp, K. C.; Perman, J. A.; Bourlinos, A. B.; Kim, K. S.; Zboril, R. Noncovalent Functionalization of Graphene and Graphene Oxide for Energy Materials, Biosensing, Catalytic, and Biomedical Applications. *Chem. Rev.* **2016**, *116*, 5464−5519.

(12) Tiwari, J. N.; Tiwari, R. N.; Singh, G.; Kim, K. S. Recent Progress in the Development of Anode and Cathode Catalysts for Direct Methanol Fuel Cells. *Nano Energy* **2013**, *2*, 553−578.

(13) Stephens, I. E. L.; Rossmeisl, J.; Chorkendorff, I. Toward Sustainable Fuel Cells. *Science* **2016**, *354*, 1378−1379.

(14) Tiwari, J. N.; Tiwari, R. N.; Kim, K. S. Zero-dimensional, one-dimensional, two-dimensional and Three-Dimensional Nanostructured Materials for Advanced Electrochemical Energy Devices. *Prog. Mater. Sci.* **2012**, *57*, 724−803.

(15) Zhang, L.; Roling, L. T.; Wang, X.; Vara, M.; Chi, M.; Liu, J.; Choi, S. I.; Park, J.; Herron, J. A.; Xie, Z. Y. Platinum-based Nanocages with Subnanometer-thick Walls and Well-defined, Controllable Facets. *Science* **2015**, *349*, 412−416.

(16) Lim, B.; Jiang, M. J. P.; Cho, E. C.; Tao, J.; Lu, X. M.; Zhu, Y. M.; Xia, Y. N. Pd−Pt Bimetallic Nanodendrites with High Activity for Oxygen Reduction. *Science* **2009**, *324*, 1302−1305.

(17) Gilroy, K. D.; Ruditskiy, A.; Peng, H.-C.; Qin, D.; Xia, Y. Bimetallic Nanocrystals: Syntheses, Properties, and Applications. *Chem. Rev.* **2016**, *116*, 10414−10472.

(18) Scofield, M. E.; Koenigsmann, C.; Wang, L.; Liu, H. Q.; Wong, S. S. Tailoring the Composition of Ultrathin, Ternary Alloy PtRuFe Nanowires for the Methanol Oxidation Reaction and Formic Acid Oxidation Reaction. *Energy Environ. Sci.* **2015**, *8*, 350−363.

(19) Du, X. X.; He, Y.; Wang, X. X.; Wang, J. N. Fine-Grained and Fully Ordered Intermetallic PtFe Catalyst with Largely Enhanced Catalytic Activity and Durability. *Energy Environ. Sci.* **2016**, *9*, 2623−2632.

(20) Chen, C.; Kang, Y.; Huo, Z.; Zhu, Z.; Huang, W.; Xin, H. L.; Snyder, J. D.; Li, D.; Herron, J. A.; Mavrikakis, M.; Chi, M.; More, K. L.; Li, Y.; Markovic, N. M.; Somorjai, G. A.; Yang, P.; Stamenkovic, V. R. Highly Crystalline Multimetallic Nanoframes with Three-Dimensional Electrocatalytic Surfaces. *Science* **2014**, *343*, 1339−1343.

(21) Poznyak, S. K.; Kulak, A. I. Characterization and Photoelectrochemical Properties of Nanocrystalline In$_2$O$_3$ Film Electrodes. *Electrochim. Acta* **2000**, *45*, 1595−1605.

(22) Jia, F.; Sun, W.; Zhang, J. H.; Li, Y. F.; Yang, B. A Facile Approach to Fabricate Three-Dimensional Ordered Macroporous Rutile Titania at Low Calcination Temperature. *J. Mater. Chem.* **2012**, *22*, 2435−2441.

(23) Tiwari, J. N.; Nath, K.; Kumar, S.; Tiwari, R. N.; Kemp, K. C.; Le, N. H.; Youn, D. H.; Lee, J. S.; Kim, K. S. Stable Platinum Nanoclusters on Genomic DNA−Graphene Oxide with a High Oxygen Reduction Reaction Activity. *Nat. Commun.* **2013**, *4*, 2221.

(24) Tiwari, J. N.; Kemp, K. C.; Nath, K.; Tiwari, R. N.; Nam, H. G.; Kim, K. S. Interconnected Pt-Nanodendrite/DNA/Reduced-Graphene-Oxide Hybrid Showing Remarkable Oxygen Reduction Activity and Stability. *ACS Nano* **2013**, *7*, 9223−9231.

(25) Loukrakpam, R.; Luo, J.; He, T.; Chen, Y.; Xu, Z.; Njoki, P. N.; Wanjala, B. N.; Fang, B.; Mott, D.; Yin, J.; Klar, J.; Powell, B.; Zhong, C. J. Nanoengineered PtCo and PtNi Catalysts for Oxygen Reduction Reaction: An Assessment of the Structural and Electrocatalytic Properties. *J. Phys. Chem. C* **2011**, *115*, 1682−1694.

(26) Gomes, J. F.; Bergamaski, K.; Pinto, M. F. S.; Miranda, P. B. Reaction Intermediates of Ethanol Electro-oxidation on Platinum Investigated by SFG Spectroscopy. *J. Catal.* **2013**, *302*, 67−82.

(27) Tiwari, J. N.; Tiwari, R. N.; Chang, Y. M.; Lin, K. L. A Promising Approach to the Synthesis of 3D Nanoporous Graphitic Carbon as a Unique Electrocatalyst Support for Methanol Oxidation. *ChemSusChem* **2010**, *3*, 460−466.

(28) Tiwari, J. N.; Tiwari, R. N.; Lin, K.-L. Controlled Synthesis and Growth of Perfect Platinum Nanocubes Using a Pair of Low-Resistivity Fastened Silicon Wafers and Their Electrocatalytic Properties. *Nano Res.* **2011**, *4*, 541−549.

(29) Wang, G.; Huang, B.; Xiao, L.; Ren, Z.; Chen, H.; Wang, D.; Abruña, H. D.; Lu, J.; Zhuang, L. Pt Skin on AuCu Intermetallic Substrate: A Strategy to Maximize Pt Utilization for Fuel Cells. *J. Am. Chem. Soc.* **2014**, *136*, 9643−9649.

(30) Gasteiger, H. A.; Kocha, S. S.; Sompalli, B.; Wagner, F. T. Activity Benchmarks and Requirements for Pt, Pt-alloy, and non-Pt Oxygen Reduction Catalysts for PEMFCs. *Appl. Catal., B* **2005**, *56*, 9−35.

(31) Liu, Y.; Mustain, W. E. High Stability, High Activity Pt/ITO Oxygen Reduction Electrocatalysts. *J. Am. Chem. Soc.* **2013**, *135*, 530−533.

(32) Shrestha, S.; Liu, Y.; Mustain, W. E. Electrocatalytic Activity and Stability of Pt Clusters on State−of−the−art Supports: A Review. *Catal. Rev.: Sci. Eng.* **2011**, *53*, 256−336.

(33) Darling, R. M.; Meyers, J. P. Mathematical Model of Platinum Movement in PEM Fuel Cells. *J. Electrochem. Soc.* **2005**, *152*, A242−A247.